第43卷第5期
2024年10月

红外与毫米波学报
J. Infrared Millim. Waves

Vol. 43，No. 5
October，2024

文章编号：1001-9014(2024)05-0595-08 **DOI**:10. 11972/j. issn. 1001-9014. 2024. 05. 002

Research on the correlation between the dual diffusion behavior of zinc in InGaAs/InP single-photon avalanche photodiodes and device performance

LIU Mao-Fan[1,2,3]， YU Chun-Lei[2,3*]， MA Ying-Jie[2,3]， YU Yi-Zhen[2,3]， YANG Bo[2,3]， TIAN Yu[2,3]，
BAO Peng-Fei[2,3]， CAO Jia-Sheng[2,3]， LIU Yi[2,3]， LI Xue[1,2,3*]

（1. Shanghai University，Shanghai 201899，China；
2. State Key Laboratories of Transducer Technology，Shanghai Institute of Technical Physics，
Chinese Academy of Sciences，Shanghai 200083，China；
3. Key Laboratory of Infrared Imaging Materials and Detectors，Chinese Academy of Sciences，
Shanghai 200083，China）

Abstract：The development of InGaAs/InP single-photon avalanche photodiodes（SPADs）necessitates the utilization of a two-element diffusion technique to achieve accurate manipulation of the multiplication width and the distribution of its electric field. Regarding the issue of accurately predicting the depth of diffusion in InGaAs/InP SPAD，simulation analysis and device development were carried out，focusing on the dual diffusion behavior of zinc atoms. A formula of $X_j = k\sqrt{t - t_0} + c$ to quantitatively predict the diffusion depth is obtained by fitting the simulated twice-diffusion depths based on a two-dimensional（2D）model. The 2D impurity morphologies and the one-dimensional impurity profiles for the dual-diffused region are characterized by using scanning electron microscopy and secondary ion mass spectrometry as a function of the diffusion depth，respectively. InGaAs/InP SPAD devices with different dual-diffusion conditions are also fabricated，which show breakdown behaviors are well consistent with the simulated results under the same junction geometries. The dark count rate（DCR）of the device decreased as the multiplication width increased，as indicated by the results. DCRs of 2×10^6，1×10^5，4×10^4，and 2×10^4 were achieved at temperatures of 300 K，273 K，263 K，and 253 K，respectively，with a bias voltage of 3 V，when the multiplication width was 1. 5 μm. These results demonstrate an effective prediction route for accurately controlling the dual-diffused zinc junction geometry in InP-based planar device processing.

Key words：InGaAs/InP single-photon avalanche photodiode，diffusion depth，znic diffusion，dark count rate

InGaAs/InP单光子雪崩光电二极管中锌的双扩散行为与器件性能关联性研究

刘茂繁[1,2,3]， 于春蕾[2,3*]， 马英杰[2,3]， 于一榛[2,3]， 杨 波[2,3]， 田 宇[2,3]， 宝鹏飞[2,3]，
曹嘉晟[2,3]， 刘 奕[2,3]， 李 雪[1,2,3*]

(1. 上海大学,上海 201899;
2. 中国科学院上海技术物理研究所 传感技术国家重点实验室,上海 200083;
3. 中国科学院红外成像材料与器件重点实验室,上海 200083)

摘要:InGaAs/InP单光子雪崩二极管(SPAD)研制需要采用两次元素扩散方法,以实现对倍增层厚度以及电场分布的精确控制。针对两次扩散深度的有效预测问题,围绕InGaAs/InP SPAD中锌原子的两次扩散行为开展了仿真分析和器件研制。基于二维模型拟合模拟的两次扩散深度,建立了预测扩散深度的公式$X_j = k\sqrt{t - t_0} + c$。利用扫描电子显微镜和二次离子质谱表征器件双扩散区的二维杂质形态和一维杂质分布,制备了不同扩散组合多种倍增层厚度的InGaAs/InP SPAD器件,各倍增层厚度与实测击穿电压呈现线性关系,击穿电压与仿真结果具有良好的一致性。根据器件暗计数率(DCR)结果,提高倍增层厚度减小了器件DCR。

Received date：2024-01-25，**revised date**：2024-06-25 **收稿日期**:2024-01-25,**修回日期**:2024-06-25

Foundation items：Supported by Shanghai Natural Science Foundation（22ZR1472600）.

Biography：LIU Maofan（2000-），male，Shanghai，master degree candidate. Research area involves InGaAs avalanche photodetectors. E-mail：2356907307@shu. edu. cn.

[*] **Corresponding authors**：E-mail：yuchunlei@mail. sitp. ac. cn，lixue@mail. sitp. ac. cn.

在倍增层厚度为1.5 μm时，过偏压3 V下温度为300 K、273 K、263 K、253 K时，分别具有2×10^6、1×10^5、4×10^4、2×10^4的DCR。这些结果证明，在基于InP的平面器件处理中精确控制双扩散锌结几何形状的有效预测路线。

关　键　词：InGaAs/InP单光子雪崩二极管；扩散深度；锌扩散；暗计数率

中图分类号：TN304　　　　**文献标识码**：A

Introduction

In recent years, planar single-photon avalanche diodes (SPADs), sometimes referred to as planar Geiger-mode avalanche photodiodes (GM-APDs), have been extensively utilized in several disciplines, including quantum key distribution (QKD), quantum imaging, and three-dimensional laser detection and ranging (LADAR)[1-5]. SPADs that utilize the InGaAs/InP material system exhibit exceptional sensitivity at the single-photon level within the near-infrared (NIR) range of 900-1700 nm. Consequently, they are regarded as very promising detectors for single-photon detection within the short-wave infrared (SWIR) spectrum [6-11]. SPADs function at voltages over the threshold for avalanche breakdown, operating in Geiger mode. The disparity between the operating voltage and the breakdown voltage in Geiger mode is denoted as the excess bias. Dark counting rate (DCR), photon detection efficiency (PDE), and afterpulse probability are crucial metrics that characterize the operation of SPADs. The width of the multiplication region has a substantial impact on PDE, DCR, and afterpulse probability [13-17]. Conventional InP-based SPADs that are fabricated utilizing double diffusion techniques successfully lower the electric field at the edges of the InP p-region. This helps to prevent premature breakdown in the multiplication area and enhances the likelihood of avalanche events occurring at the center of the multiplication region [12]. The extent of Zn diffusion in the double diffusion process has a direct impact on the multiplication width (MW), whereas shallow diffusion is essential for minimizing the electric field at the edges. Hence, achieving accurate manipulation of the dual diffusion behavior is crucial in the production of high-performance devices.

The prevailing configuration of InGaAs/InP SPADs is the Separate Absorption Grading Charge Multiplication (SAGCM) structure, which is distinguished by the distinct segregation of the multiplication zone and the absorption region. The P+ active area in the InP cap layer is created via diffusion. The double diffusion structure is initially created with a shallow depth using the first mask, and subsequently, a deep diffusion structure is formed with a greater depth using the second mask. The double Zn diffusion structure enhances the concentration of the intense electric field needed for avalanche breakdown in the multiplication zone, facilitating the detection of large-scale signals and the efficient identification of photo-generated carriers. A 2013 study conducted by Politecnico di Milano analyzed the influence of multiplier layers on the efficiency of InGaAs/InP SPAD devices [14]. The study demonstrated that diminishing the MW led to a decline in the breakdown voltage. Furthermore, PDE and DCR both showed a progressive rise as the MW dropped. In 2016, the University of Science and Technology of China did an analysis on how the multiplier layer affects the performance of InGaAs/InP SPAD devices[18]. The investigation demonstrated a robust association between the MW and the performance of PDE and DCR. While numerous theoretical studies have been published on the impact of the MW [13-18], there is a scarcity of papers about the prediction of the multiplier layer's width.

The diffusion process becomes increasingly intricate when the SPADs undergo two sequential diffusion stages, with deep diffusion following shallow diffusion. As a result, the fitting of the two diffusion depths is distinct from single-step diffusion.

This paper employs numerical simulations to forecast the diffusion patterns that occur in two distinct steps. The characterization of diffusion depth in experiments is achieved by the utilization of SEM and SIMS. By integrating simulation and experimental data, a very accurate predictive model for profound diffusion depth has been established. The functionality of devices with various dual diffusion architectures was examined and studied in both linear and Geiger modes. Precise regulation of the depth of diffusion is crucial for attaining superior performance in InGaAs/InP SPADs.

1 Device structure design

Figure 1(a) displays the cross-sectional schematic diagram of the double diffusion InGaAs/InP SAGCM SPAD structure. The device structure, starting from the bottom and moving upwards, comprises a substrate made of n-type InP with metallization, followed by an n-type InP buffer layer, an unintentionally-doped (uid) absorption layer made of InGaAs, an n-type InGaAsP grading layer, a moderately doped n-type InP charge layer, and finally an uid InP cap layer that includes a multiplication layer. The experiment involved the design of four sets of devices, each with fixed shallow diffusion times and different deep diffusion times. Fig. 1(b) displays the schematic design of the first shallow diffusion profile. In this diagram, X_{j1} denotes the distance of the shallow diffusion from the InP/SiNx surface. The schematic diagram of the structure after double diffusion is shown in Fig. 1(a). In this context, X_{j2} denotes the shallow diffusion distance following deep diffusion, while X_{j3} indicates the deep diffusion distance. The value of X_{j4} is determined by subtracting X_{j1} from X_{j2} in order to precisely define the re-diffusion process. The multiplication layer is situated underneath the deep diffusion region and functions as the major zone for impact ionization. The cap layer thickness is subtracted from the deep diffusion distance to obtain MW. The correlation between the depth of diffusion and the width of the multiplier is clearly apparent. In shallow diffusion, a p-type floating guard ring is added near the boundary to further reduce the strength of the electric field at the edge of the device.

2 Simulations and results

2.1 Study of diffusion process

2.1.1 Physical model of diffusion simulation

This work utilized a Two-Dimensional Model [19-20] for simulating the device diffusion process. This model implies a unidirectional link between defects and dopants, where the diffusion of dopants is greatly influenced by point defects, while the diffusion of point defects is thought to have no connection to the dopant diffusion process. During this diffusion process, it is presumed that there is an excess of point defects, suggesting that the diffusion process is not in a state of thermal equilibrium. The equation governing the continuation of dopants is as follows:

$$\frac{\partial C_{ch}}{\partial t} = -\sum_{X=I,V} \nabla \cdot J_{AX} \quad , \quad (1)$$

$$J_{AX} = -f_x D_{AX}\left[\nabla\left(C_A \frac{C_X}{C_X^*}\right) - Z_A\left(C_A \frac{C_X}{C_X^*}\right)\frac{QE}{KT}\right] \quad , \quad (2)$$

where C_I and C_V represent the actual concentrations of interstitials and vacancies, while C_I^* and C_V^* represent the equilibrium concentrations. The f_x is an empirical defect factor. Excess point defects will affect the dopant diffusion coefficient through a simple proportionality factor.

$$\frac{\partial C_I}{\partial t} = -\nabla \cdot J_I - R_B + R_T - R_{\langle 311 \rangle} \quad , \quad (3)$$

$$\frac{\partial C_V}{\partial t} = -\nabla \cdot J_V - R_B \quad , \quad (4)$$

R_B represents the bulk recombination rate, R_T represents trap capture or release by interstitials, and $R_{\langle 311 \rangle}$ represents interstitial aggregation.

2.1.2 Diffusion process simulation results

During the simulation procedure, the initial step involved etching the bigger mask to generate a diffusion structure with a relatively shallow depth. Afterwards, the smaller mask was etched to generate a profound diffusion structure with increased depth. Fig. 2 below illustrates the 2D double-diffused SPAD structure used for device simulation.

In Fig. 3, the diffusion depth is defined as the distance at which the doping concentration is equal to the background concentration. The deep diffusion distance X_{j3}, which corresponds to various deep diffusion durations, was determined using fitting analysis, as depicted in Fig. 4. It was observed that the fitting relationship followed the formula $X = k\sqrt{t} + c$. In this context, the variable k indicates the diffusion coefficient, whereas t represents the entire diffusion time. Deep diffusion is distinct from typical single-step diffusion because it is rooted in shallow diffusion. Thus, a constant c was included to calibrate the deep diffusion process, taking into account its deviation from single-step diffusion.

Upon comparing the diffusion state contours depicted in Fig. 2, it becomes evident that there is a substantial increase in the depth of the guard ring. However, the diffusion mask of the guard ring lacks a diffusion source during the deep diffusion phase. The increased depth of the guard ring diffusion is a result of re-diffusion caused by temperature. After conducting an analysis of the guard ring's surface Zn concentration following both shallow and deep diffusion, it was determined that the surface concentration after shallow diffusion is 10^{19} cm^{-3}, whereas after deep diffusion, it is around 6×10^{18} cm^{-3}. This verifies that the increase in the depth of the guard ring is truly a result of temperature. In addition, a surface concentration analysis was performed to examine the enhanced depth of shallow diffusion. The trend in the change in surface concentration aligns with that of the guard ring. Therefore, the increased depth of shallow diffusion can be attributed to temperature-induced re-diffusion.

When the shallow diffusion time t_1 is sufficiently short, shallow diffusion can be neglected, and instead it serves as a diffusion source for the second diffusion, with a solubility point of approximately 10^{18} cm^{-3}. Therefore, a fraction of the material (with negligible diffusion) that diffused during t_1 is considered as the source of diffusion for the second diffusion. The second diffusion depth is denoted as X_{j4}, and the corresponding time is t_2. The equation that accurately describes this process is $x =$

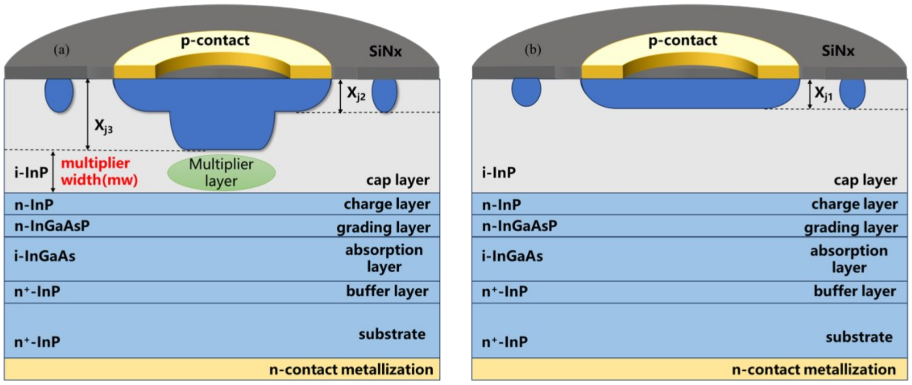

Fig. 1 Two-dimensional structure of double-diffused positive-illumination InGaAs/InP SAGCM: (a) structure after deep diffusion is complete; (b) structure after shallow diffusion is complete

图 1 双扩散正照明 InGaAs/InP SAGCM 的二维结构：(a) 深扩散完成后的结构；(b) 浅扩散完成后的结构

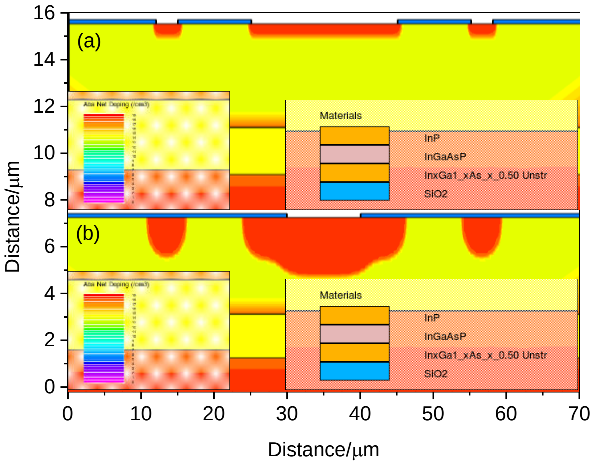

Fig. 2 The simulation of diffusion profile: (a) contour after shallow diffusion; (b) contour after deep diffusion
图2 扩散剖面的模拟:(a)浅扩散完成后的轮廓;(b)深扩散完成后的轮廓

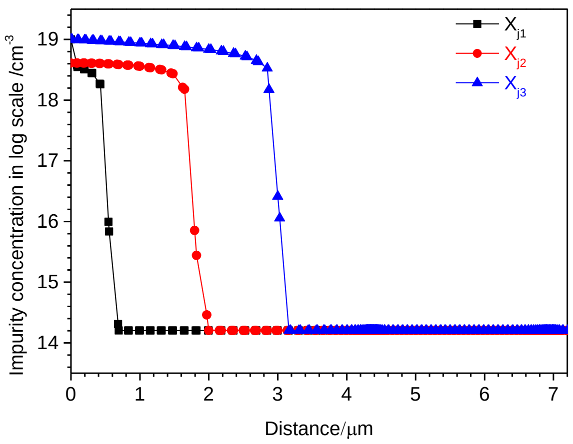

Fig. 3 Distribution of Zn impurity concentration in InP
图3 InP中Zn杂质浓度的分布

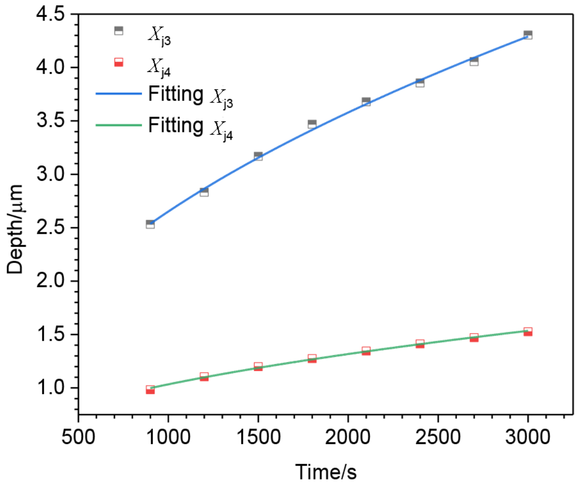

Fig. 4 Fitting curves for X_{j3} and X_{j4}
图4 X_{j3}和XX_{j4}的拟合曲线

$k\sqrt{t}+c$. Considering it as a solitary diffusion process[23], the behavior of x can be described by the equation $x=k\sqrt{t}$. However, it should be noted that this formula alone does not provide complete accuracy. Since the first diffusion serves as the diffusion source and eliminates any surface conditions, there is no need to take interface circumstances into account. In order to offset this effect, a constant c is used to modify the formula. Consequently, shallow diffusion may be conceptualized as consisting of two distinct diffusion processes: the initial diffusion depth can be accurately estimated using the usual formula $x=k\sqrt{t}$, while the subsequent diffusion is a result of temperature-induced re-diffusion, which can be anticipated using the aforementioned fitting formula.

2.1.3 Fitting of deep diffusion depth

The experimental portion involved the fabrication of devices with varying diffusion times using a two-step sealed ampoule zinc diffusion technique. The experiment entailed creating four sets of devices with consistent shallow diffusion times and different deep diffusion times. The SEM and SIMS methods were employed to characterize and assess the diffusion profile and depth.

The experiments rigorously adhered to the same approach as the simulation. Initially, the first mask created a diffusion structure that was relatively shallow. Following that, a more profound diffusion structure was formed utilizing the second mask. The shallow diffusion time was set at a constant duration of 7.5 minutes, whereas four distinct durations were employed for deep diffusion: 15 minutes, 22 minutes, 29 minutes, and 36 minutes. SEM and SIMS tests were performed on the manufactured devices, and the outcomes of the testing are displayed in Fig. 5.

Securely affix the sample to a sample stage using conductive adhesive. Subsequently, insert it into the scanning electron microscope (SEM) system for the purpose of conducting tests. Modify the contrast and brightness of the image, as exemplified in the picture. The region exhibiting the greatest luminosity corresponds to the double diffusion area that encompasses the Zn element. The SEM studies revealed diffusion depths of 2.010 μm, 2.689 μm, 3.231 μm, and 3.638 μm.

By harnessing the heightened sensitivity of sims ions, it is feasible to accurately measure the exact depth of the Zn element in the diffused sample. This enables the measurement of the extent of profound diffusion within the device. The SIMS measurements resulted in diffusion depths of 1.83 μm, 2.46 μm, 2.96 μm, and 3.24 μm.

The equation shown below was constructed in order to enhance the accuracy of the fitting method for simulating deep diffusion depth: The equation $X=k\sqrt{t-t_0}+c$ illustrates the relationship between the diffusion distance X, the diffusion coefficient k, the overall diffusion time t, and the time required for the temperature to rise during the diffusion process t_0. An adjustment is required due to the temperature increase period involved in the two-step sealed ampoule zinc diffusion method. Through-

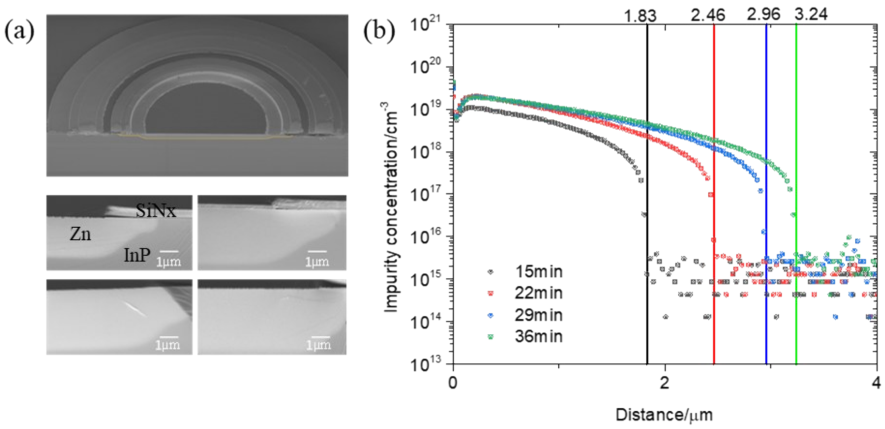

Fig. 5 Diffusion depth characterization results：(a) SEM test results；(b) SIMS test results
图5 扩散深度的表征结果：(a) SEM测试结果；(b) SIMS测试结果

out this time frame, the diffusion coefficient exhibits variations in accordance with temperature. Hence, the time interval during which the diffusion coefficient remains unchanged should not include the heating period t_0. The constant c is utilized to modify the diffusion distance throughout the heating procedure. The revised equation was utilized to accurately model the experimental data collected from both SEM and SIMS experiments. The results depicted in Fig. 6 indicate that the formula successfully matches the experimental data.

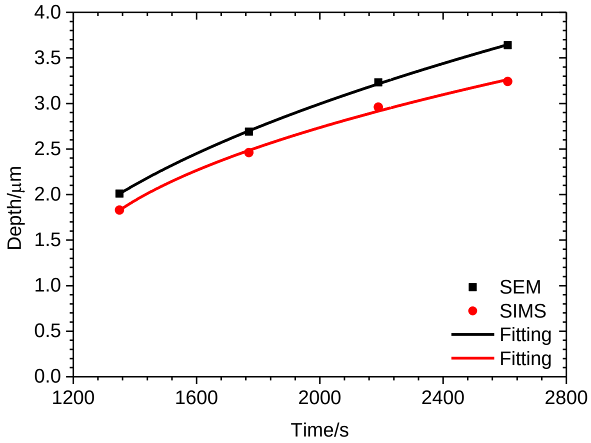

Fig. 6 Fitting results of deep diffusion depth from SEM and SIMS tests
图 6 基于SEM和SIMS测试数据深扩散深度拟合结果

2.2 Electrical performance of InGaAs APD

2.2.1 Physical model of electrical performance

In order to simulate the electrical performance of the device, we utilized carrier transport equations that are based on drift-diffusion. The models primarily consist of mobility models, Shockley-Read-Hall (SRH) recombination models, Auger recombination models, and impact ionization models. In this work, the Selberherr model, which relies on temperature and electric field, was utilized for the impact ionization model. The model presents the expressions for the electron impact ionization coefficient α_n and the hole impact ionization coefficient α_p as follows. The impact ionization parameters for the InP cap layer and InGaAs absorption layer are chosen according to the values presented in Table 1. The material parameters used for simulation were derived from the prior study [21].

$$\alpha_n = ANexp^{\left[-\left(\frac{BN}{E}\right)^{BETAN}\right]} \quad , \quad (5)$$

$$\alpha_p = APexp^{\left[-\left(\frac{BP}{E}\right)^{BETAP}\right]} \quad , \quad (6)$$

where E represents the electric field at a specific location in the structure, indicating the direction of current flow.

Table 1 Selberherr model parameters for InP/InGaAs material
表1 InP/InGaAs材料的Selberherr模型参数

Parameter	Unit	InP multiplier	InGaAs absorber
AN2	$\times10^6$ cm^{-1}	3.5	3.07
AP2	$\times10^6$ cm^{-1}	1.23	9.47
BN2	$\times10^6$ V/cm	3.5	2.54
BP2	$\times10^6$ V/cm	2.4	2.63
BERAN	–	1	1
BETAP	–	1	1

The ray tracing approach is utilized to simulate the photoelectric response of devices. The simulation was performed by inputting data such as incident angle, wavelength, intensity, and reflection into the luminous module, enabling the calculation of light ray behavior.

2.2.2 Electrical performance simulation analysis

The simulation examined the correlation between breakdown voltage and MW. Initially, the discrepancy between shallow and deep diffusion was rectified at a measurement of 1.6 μm. Subsequently, devices with different MW were simulated to analyze the distribution of the electric field, as illustrated in Fig. 7. The strong electric field is predominantly situated beneath the core deep diffusion InP region, as anticipated. The shallow diffusion region has moderate electric field intensities in its surrounding locations. The lateral electric field remains balanced with the gradient profile due to the inclusion of the guard ring. However, if the MW is excessively large, the high electric field region becomes concentrated at the margins of shallow and deep diffusion, hence increasing the likelihood of experiencing edge breakdown occurrences. Moreover, the electric field within the InGaAs absorption layer remains within the low-field regime. After doing a thorough analysis of the two-dimensional electric fields, it is evident that the electric field within the InP multiplication layer diminishes progressively as the MW increases. The device with the MW of 0.365 μm exhibits a significantly greater electric field in its core region compared to the device with the MW of 1.359 μm, with a difference of approximately $2\text{x}10^5$ V/cm.

The devices were evaluated for their photodetector performance within the linear range. Current-voltage (*I*–*V*) characteristics were measured for devices with varying MW under both lit and dark conditions at a temperature of 300 K. The results are presented in Fig. 8. To achieve illumination, a light source emitting at a wavelength of 1550 nm and an intensity of 0.1 W/cm^2 was employed. InP exhibits no light absorption within this specific range of wavelengths. Hence, the production of photocurrent signifies a reduction in the InGaAs layer. The graph illustrates the correlation between breakdown voltage, punch-through voltage (the voltage at the device's ends when the depleted region extends to the absorption layer), and MW. It is evident that the breakdown voltage (V_{BR}) does not exhibit a linear relationship with MW at all intervals. When the MW is insufficiently narrow, the depletion zone penetrates the InGaAs layer prematurely. This leads to a reduction in the partial voltage of the multiplier layer and a drop in the electric field, thus resulting in an increase in the breakdown voltage [15]. Nevertheless, the punch-through voltage (V_P) exhibits a progressive rise as the MW increases.

2.2.3 *I*–*V* characteristics of different multiplication width

MW were determined using the data obtained from the standard error of the mean (SEM) tests. Figure 9 displays a comparison between the simulated and measured dark current (*IV*) curves of four distinct MW. The photodetector characteristic curves derived from *IV* tests are displayed. Throughout the simulation, the second diffusion depth was meticulously regulated to align precisely with the results obtained from the SEM test. When simulating the electrical performance of devices, the focus is primarily on simulating their breakdown behavior. However, factors like defects and stress in the material are not considered, leading to an overly idealized simulated dark current that deviates significantly from the measured

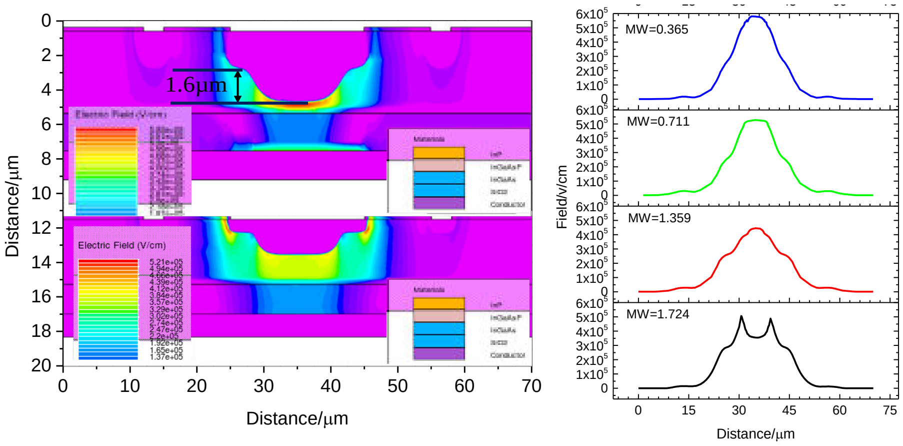

Fig. 7 Variation of electric field with different MW
图 7 不同MW的电场变化

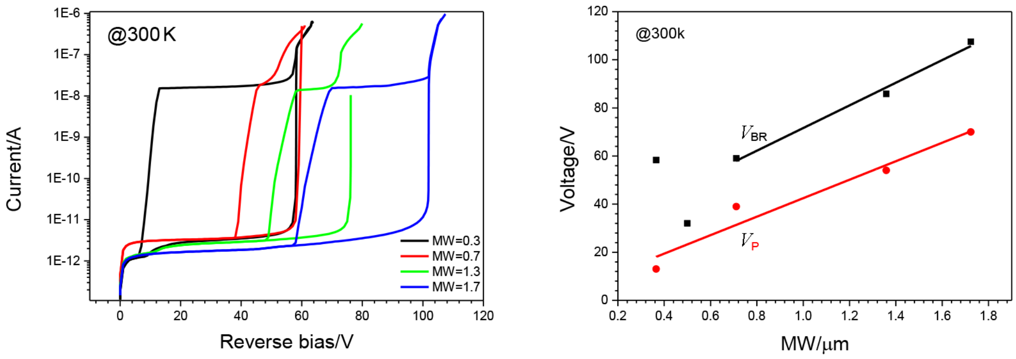

Fig. 8 Variation of breakdown voltage and punch-through voltage with different MW
图 8 不同MW击穿电压和贯穿电压的变化

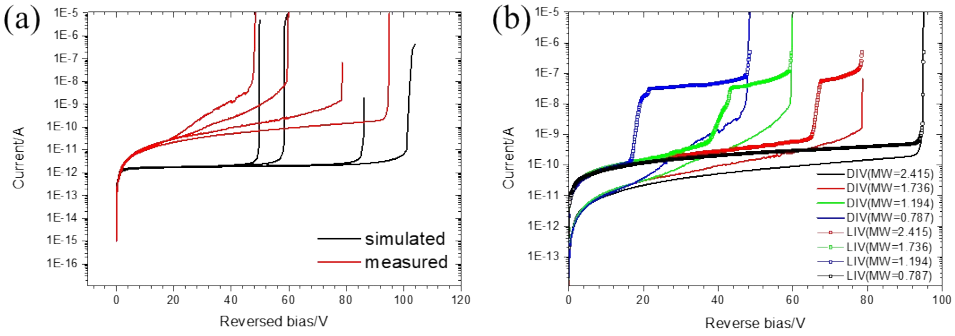

Fig. 9 Simulation and test results: (a) comparison of dark current (*IV*) simulated and measured curves; (b) photodetector characteristics curve from *IV* tests
图 9 仿真和实测结果:(a)暗电流仿真曲线和实测曲线对比;(b)*IV*测试后的光电特性曲线

dark current. Based on the *IV* test results, it can be noted that the V_{BR} (the voltage at which a current of 10 μA is reached) of the device climbs progressively when the MW is incremented, reaching values of 48.9 V, 59 V, 76.2 V, and 94.5 V, respectively. This is because an increase in MW will result in a reduction of its electric field strength. A linear correlation is established between MW and V_{BR} within a specific range of multiplication width, as illustrated in Fig. 10.

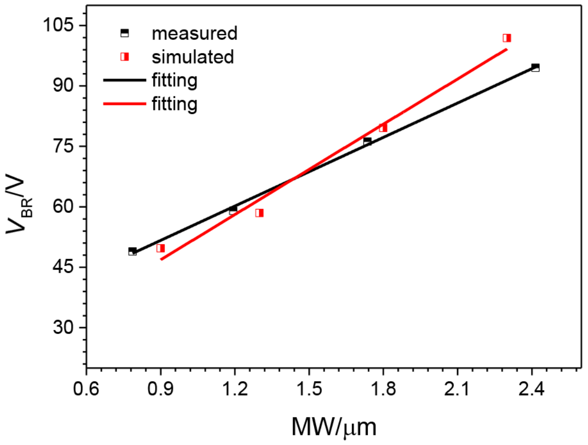

Fig. 10 Relationship between multiplication width (MW) and breakdown voltage (V_{BR})
图 10 击穿电压和倍增层宽度的关系

2.2.4 Geiger-mode characteristics testing

Geiger-mode measurements were conducted using a custom-built gating measuring system. Two devices with MW values were chosen for Geiger-mode performance evaluation, as depicted in Fig. 11. It is evident that the DCR reduces significantly as the temperature decreases. At a temperature of 300 K and with an excess bias voltage of 3.5 volts, the DCR is roughly 2×10^6 counts per second. Nevertheless, when the sample was exposed to a temperature of 253 K, the DCR increased to 2×10^4 counts per second. The decrease in dark counts is a result of the elimination of thermally produced dark counts in InGaAs and tunneling dark counts in the InP multiplication layer at lower temperatures [22]. It is worth mentioning that devices with thinner multiplication layers demonstrate elevated dark count rates at identical temperatures. At the identical temperature and excess bias voltage of 3 volts, the device with the MW of 0.8 μm exhibits a DCR that is 5×10^4 counts per second greater than the device with the MW of 1.5 μm. This phenomenon is ascribed to the intensified electric field that arises from the decrease in MW.

3 Conclusions

The primary objective of this study was to concentrate on the design of the device structure and the numerical simulation of InGaAs/InP single-photon avalanche diodes (SPADs) using both shallow and deep diffusion pro-

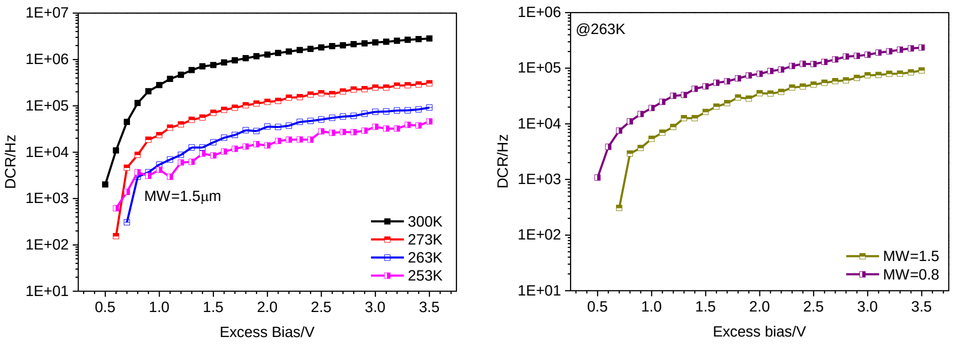

Fig. 11 Trends in Dark Count Rate (DCR) variation with temperature and MW
图 11 暗计数率随温度和MW变化的趋势

cesses. Models were created to predict the depths of diffusion in both cases. Experiments were carried out to analyze the performance of the device in both linear and Geiger modes. The research findings suggest that the prediction model for shallow diffusion depth can be regarded as a composite of an initial diffusion and a subsequent diffusion resulting from temperature. The formula $X = a\sqrt{t - t_0} + c$ can be used to fit the predictive model for deep diffusion depth. The width of the multiplication layer has a substantial impact on the electric field within the multiplication zone. The breakdown voltage exhibits an initial fall followed by an increase as the multiplication width grows. In addition, the study examined how the thickness of the multiplication layer and temperature affect the performance of Geiger mode. It was noted that decreasing the temperature significantly decreases the rate at which dark counts occur, while decreasing the thickness of the multiplication layer increases the rate at which dark counts occur. These findings are crucial reference points for developing high-performance InP near-infrared SPAD arrays, which facilitate advanced applications like high-speed quantum communication and high-resolution 3D laser imaging.

References

[1] Zhang Jun, Zbinden H, *et al.* Advances in InGaAs/InP single-photon detector systems for quantum communication [J]. *Light: Science & Applications*, 2015, **4**(5): 1-13.

[2] M. Liu, *et al.* High-Performance InGaAs/InP Single-Photon Avalanche Photodiode [J]. *IEEE Journal of Selected Topics in Quantum Electronics*, 2007, **13**(4): 887-894.

[3] Cusini I, Berretta D, Conca E, *et al.* Historical Perspectives, State of Art and Research Trends of SPAD Arrays and Their Applications (Part II: SPAD Arrays) [J]. *Frontiers in Physics*, 2022, **10**: 1-20.

[4] Aull B F, Loomis A H, Young D J, *et al.* Three-dimensional imaging with arrays of Geiger-mode avalanche photodiodes [C]. SPIE, 2004: 105-116.

[5] Yu C, Shangguan M, Xia H, *et al.* Fully integrated free-running InGaAs/InP single-photon detector for accurate lidar applications [J]. *Opt Express*, 2017, **25**(13): 14611-14620.

[6] Bruschini C, Hmoulle H, Antolovic I M, *et al.* Single-photon avalanche diode imagers in biophotonics: review and outlook [J]. *Light: Science & Applications*, 2019, **8**(1): 409-436.

[7] Sanzaro M, Calandri N, Ruggeri A, *et al.* InGaAs/InP SPAD with Monolithically Integrated Zinc-Diffused Resistor [J]. *IEEE Journal of Quantum Electronics*, 2016, **52**(7): 1-7.

[8] Jiang X, *et al.* InGaAsP - InP Avalanche Photodiodes for Single Photon Detection [J]. *IEEE Journal of Selected Topics in Quantum Electronics*, 2007, **13**(4): 895-905.

[9] Wang S, Ye H, Geng L, *et al.* Design, Fabrication, and Characteristic Analysis of 64×64 InGaAs/InP Single-Photon Avalanche Diode Array [J]. *Journal of Electronic Materials*, 2022, **51**(5): 2692-2697.

[10] Hiskett P A, Buller G S, Loudon A Y, *et al.* Performance and design of InGaAs /InP photodiodes for single-photon counting at 1.55 μm [J]. *Appl Opt*, 2000, **39**(36): 6818-6829.

[11] M. Liu, *et al.* Low Dark Count Rate and High Single-Photon Detection Efficiency Avalanche Photodiode in Geiger-Mode Operation [J]. *IEEE Photonics Technology Letters*, 2007, **19**(6): 378-80.

[12] Ma Ying-Jie, Gu Yi, Li Xue, *et al.* InGaAsP/InP Geiger-Mode Avalanche Photodiode Towards Sub-kHz Dark Count Rate at 20% Photon Detection Efficiency [J]. *Journal of Lightwave Technology*, 2022, **40**(22): 7364-7374.

[13] Mcintyre R J. Multiplication noise in uniform avalanche diodes [J]. *IEEE Transactions on Electron Devices*, 1966, ED-13(1): 164-168.

[14] Acerbi F, Anti M, Tosi A, *et al.* Design Criteria for InGaAs/InP Single-Photon Avalanche Diode [J]. *IEEE Photonics Journal*, 2013, **5**(2): 6800209.

[15] Kiwon L, Kyounghoon Y. Analysis of InGaAs/InP Single-Photon Avalanche Diodes With the Multiplication Width Variation [J]. *IEEE Photonics Technology Letters*, 2014, **26**(10): 999-1002.

[16] Preobrazhenskii V V, Chistokhin I B, Putyato M A, *et al.* Single Photon Detectors Based on InP/InGaAs/InP Avalanche Photodiodes [J]. *Optoelectronics, Instrumentation and Data Processing*, 2022, **57**(5): 485-493.

[17] Walker A W, *et al.* Zn diffusion depth effect on photoresponse uniformity in InP/InGaAs avalanche photodiodes [J]. *Optical and Quantum Electronics*, 2022, **54**(9): 573.

[18] MA J, BAI B, WANG L J, *et al.* Design considerations of high-performance InGaAs/InP single-photon avalanche diodes for quantum key distribution[J]. *Appl Opt*, 2016, **55**(27): 7497-502.

[19] Mathiot D, Pfister J C. Dopant diffusion in silicon: A consistent view involving nonequilibrium defects [J]. *Journal of Applied Physics*, 1984, **55**(10): 3518-3530.

[20] Fahey P M, Griffin P B, Plummer J D. Point defects and dopant diffusion in silicon [J]. *Reviews of Modern Physics*, 1989, **61**(2): 289-384.

[21] Yuan P, Hansing C C, Anselm K A, *et al.* Impact ionization characteristics of III-V semiconductors for a wide range of multiplication region thicknesses [J]. *IEEE Journal of Quantum Electronics*, 2000, **36**(2): 198-204.

[22] Donnelly J P, Duerr E K, Mcintosh K A, *et al.* Design Considerations for 1.06-um InGaAsP - InP Geiger-Mode Avalanche Photodiodes [J]. *IEEE Journal of Quantum Electronics*, 2006, **42**(8): 797-809.

[23] Ettenberg M H, Lange M J, Sugg A R, *et al.* Zinc diffusion in InAsP/InGaAs heterostructures [J]. *Journal of Electronic Materials*, 1999, **28**(12): 1433-1439.